Received August 27, 2021, accepted September 8, 2021, date of publication September 13, 2021,
date of current version September 20, 2021.

Digital Object Identifier 10.1109/ACCESS.2021.3112224

Field Reconstruction for Modeling Multiple Faults in Permanent Magnet Synchronous Motors in Transient States

SVEINUNG ATTESTOG, HUYNH VAN KHANG, AND KJELL G. ROBBERSMYR, (Senior Member, IEEE)
Department of Engineering Sciences, University of Agder, 4879 Grimstad, Norway
Corresponding author: Sveinung Attestog (sveinung.attestog@uia.no)

ABSTRACT Conventional field reconstruction model (FRM) for electrical machines has proved its main strength in efficient computations of magnetic fields and forces in healthy permanent magnet synchronous machines (PMSM) or faulty machines in steady states. This study aims to develop a magnet library of different magnet defects and include inter-turn short-circuit (ITSC) in the FRM for PMSM. The developed FRM can model a combination fault between ITSC, and magnet defect in a PMSM in transient states. Within the framework, an 8-turn ITSC was modelled in both finite element analysis (FEA) and FRM, and then identified by the extended Park's vector approach. The air-gap magnetic field reproduced by the FRM shows a good agreement with the result from time-stepping FEA. The computation speed is over 1000 times faster than an equivalent time-stepping FEA. The suggested FRM allows for quickly understanding effect of faults in the rotor and stator on the air-gap magnetic flux density and identifying unique signatures for such defects.

INDEX TERMS Demagnetisation, field reconstruction, inter-turn short circuit, permanent magnet synchronous motor.

I. INTRODUCTION

Modelling and simulation allow for a profound understanding of electrical machines in healthy and faulty conditions. Usually, modelling of electrical machines requires a trade-off among computational burden, complexity and accuracy. Electrical equivalent circuit (EEC), winding function theory, magnetic equivalent circuit, and finite element analysis (FEA) have been the most common modelling methods for electrical machines for many decades. One modelling strategy of creating new models is to modify previous models to include more physical phenomena. The other one is to combine two modelling techniques to obtain individual merits or compensate for any shortcoming in each method. Among others, field reconstruction model (FRM) is very efficient in computing magnetic fields and forces in electrical machines [1]. This method was first developed about one and a half decades ago, being briefly discussed hereafter.

The FRM technique recreates the airgap magnetic flux density by superimposing and phase-shifting the radial and tangential components of magnetic flux density, exported from the static FEA. It maintains the accuracy of FEA, but is significantly faster to compute, especially in time-stepping simulation or solving multi-physics problems. The authors in [2] investigated the vibration level of a permanent magnet synchronous motor (PMSM) at different speeds, and loads in steady-state conditions. Within the work, each fault scenario required a computation time of 70 min in FRM, while the equivalent FEA would require 100 days. The authors in [3] published many papers on using FRM to deal with fault detection of five-phase PMSMs and optimal current excitation.

Conventional FRMs have two variable inputs: rotor position and currents. This linear model fits well surface-mounted permanent magnet synchronous motor (SPMSM) because those machines do not work much in saturation conditions. The conventional FRMs [4] must respect the following assumptions:

- No deformation in stator or rotor core structures due to internal forces
- No saturation condition
- Zero flux density in the axial direction

The associate editor coordinating the review of this manuscript and approving it for publication was Zhuang Xu.

- No end-coil effect
- Hysteresis and eddy currents are neglected

To improve the existing FRMs, three versions of the FRMs have been proposed in [5]–[7] during the last decade. These FRMs included the interaction between the magnets and stator teeth, and slotting effect. The first one combined relative and differential permeabilities, being obtained numerically in static FEA. The second one simplified the motor geometry by employing conformal mapping and transforming the slotted stator to a slotless stator. However, the permeability in the airgap requires a more complicated equation, depending on the x- and y-coordinate. The last one considers the slotting effect and non-linear material by computing the basis functions at different rotor positions and current excitation. A look-up table is generated from the static FEAs. This allows the FRM to model interior permanent magnet synchronous motors. Towards fault diagnosis, the authors in [8] predicted partial demagnetisation and static eccentricity by FRM. In this framework of static eccentricity, the non-uniform airgap has to be taken into account by generating the basis functions for each stator phase separately, and then computing the rotor basis function for all rotor positions. To our best knowledge, no existing FRM is able to model multiple faults in a SPMSM in transient states.

This work aims to develop a FRM for modelling SPMSMs in transient states, allowing for quickly investigating multiple faults in dynamic operations. The first contribution is to build a magnet library for the FRM to model SPMSMs in faulty conditions. One magnet is quickly studied at a time in static FEAs. The suggested library consists of several faulty magnets, which can be combined in any way for recreating the rotor basis functions for the FRM. The second contribution is to include the effect of short circuit in the FRM. A FRM was initially used for detecting inter-turn short circuit (ITSC) in five-phase machines [9], but to the authors' knowledge, this has not been fully explored in transient states or mixed faults. The two modifications allow the proposed FRM to model SPMSMs with combined magnet defects and inter-turn short circuit in transient states. The performance of the proposed FRM is verified by using time-stepping FEA.

II. DEVELOPED FIELD RECONSTRUCTION MODEL

The principle of the FRM is to create a set of basic functions for the magnetic field in the airgap. In case of SPMSMs, this includes the magnets in the rotor and armature current in the stator. They are studied separately and exported from static FEAs and later superimposed in the FRM [10].

$$\begin{aligned} B_N(\theta+\theta_m, I(t)) &= B_{nPM}(\theta+\theta_m) + B_{nS}(\theta, I(t)) \\ B_T(\theta+\theta_m, I(t)) &= B_{tPM}(\theta+\theta_m) + B_{tS}(\theta, I(t)). \end{aligned} \quad (1)$$

The basis functions are extracted from the airgap at the distance R from the center. The static FEA generates the x- and y-components of the flux density, but they need to be converted to polar coordinate r and θ for the FRM. However, the rotor basis function is phase shifted by the rotor position θ_m. The exported functions of flux density depend on both r and θ. For a simplification, r is chosen to be constant, thus is not needed in the description in (1). The stator basis function is excited by the three phase currents $I_a(t)$, $I_b(t)$, and $I_c(t)$ represented by $I(t)$ in (1). A block diagram of the proposed FRM is shown in Fig. 1.

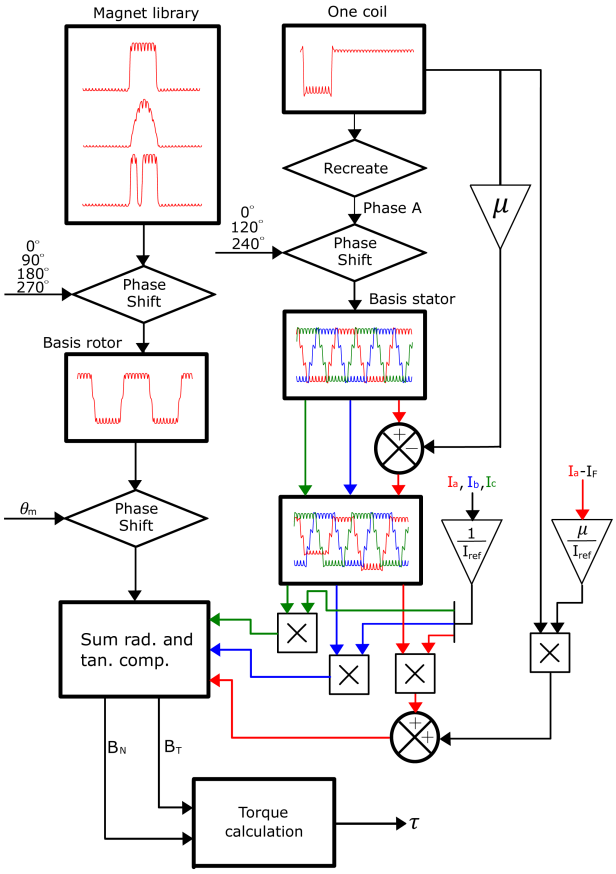

FIGURE 1. The suggested diagram of field reconstruction model.

A. ROTOR BASIS FUNCTION AND MAGNET LIBRARY

The rotor basis function is obtained by setting the phase currents to 0 A. Conventionally, all the magnets are defined in FEA when computing the rotor basis function. It is proposed to only let one of the magnets be active and export radial ($B_{r1PM,k}$) and tangential ($B_{t1PM,k}$) components for the single magnet basis functions to the FRM. The complete rotor basis functions (B_{rPM} and B_{tPM}) are then recreated in (2).

$$\begin{aligned} B_{rPM}(\theta) &= \sum_{k=1}^{2p} (-1)^{k-1} B_{r1PM,k}\left(\theta + \frac{\pi(k-1)}{p}\right) \\ B_{tPM}(\theta) &= \sum_{k=1}^{2p} (-1)^{k-1} B_{t1PM,k}\left(\theta + \frac{\pi(k-1)}{p}\right), \end{aligned} \quad (2)$$

The integer $k = [1, 2p]$, where p is the pole pair. In this study, a north pole was selected as the active magnet, but the south pole can easily be computed by multiplying with -1.

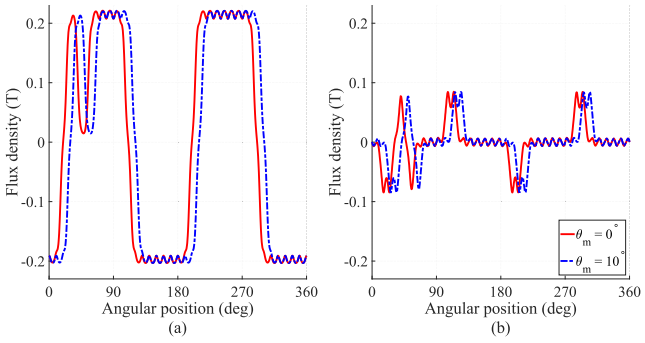

FIGURE 2. Recreated rotor function at two different rotor positions with parts removed from one magnet, (a) radial component and (b) tangential component.

The sign of the magnets is taken into consideration in (2), but is not included in Fig. 1. A collection of individual magnet basis functions with different defects is put into the magnet library. The radial components of different magnets are shown in the top left corner of Fig. 1, but both radial and tangential components are included in pairs. Any magnet can be replaced with any term in (2), thus any sets of magnets can be combined and rearranged in the FRM without the need to study every set in static FEAs. This is very time-saving in term of combinatorics and factorial function. Fig. 2 shows the magnetic flux density at the rotor positions of 0° and 10°, being as an example of a reconstructed rotor including three healthy magnets and one faulty magnet, in which a piece is missing [11].

The single magnet basis function is computed at multiple angles of 1° increment in the interval [0°, 10°], being used as a look-up table in the model. The contribution from the rotor is computed by interpolation in the look-up table at an angle between 0° and 10°. This angle is the remainder after subtracting the position θ_m by the closest multiple of slot pitch (10° for 36 slots motor), which is still smaller than θ_m. The output function is phase-shifted by that slot pitch multiple. Switching the order between these two operations will increase the computational burden. For example, when $\theta_m = 73.6°$, a function is extracted by interpolating between 3° and 4°, then phase-shifting that output function by 70°. The purpose of the look-up table is to include the slotting effect as described in [7].

The phase-shift process is conducted by removing parts of the basis function vector at the beginning, which are added at the end or in the other way around, depending on the direction of rotation. This can be done by using a look-up table. The rotor basis functions are repeated two times in the interval of $[0, 4\pi]$. The air-gap field basis function is extracted with an interpolation for the interval of $[\theta_{r,min}, \theta_{r,min} + 2\pi]$. The angle $\theta_{r,min}$ equals θ_m mod 360°. In other words, the smallest positive remainder of the fraction is $\frac{\theta_m}{360°}$.

The accuracy of a FRM significantly depends on the original static FEA. The mesh in the model can affect the final FRM. It is important to select the number of elements along the air-gap equal to a multiple of 360° divided by the angular increment. This will ensure that the meshes in the rotor and stator will perfectly align in every increment. The rotor basis function will become noisy due to interpolation performed in FEA if the nodes of the rotor and stator meshes are not perfectly aligned.

B. STATOR BASIS FUNCTION AND INTER-TURN SHORT CIRCUIT

The conventional FRMs place only one wire in a stator slot with a current of 1 A [10], and the stator basis function is recreated by phase-shifting and superimposition with respect to winding distribution. When developing this model, placing only one wire did not produce the accurate reproduction of the magnetic flux in the air-gap. The motor studied in this paper has concentrated windings, thus a coil of 80 turns occupying two stator slots is used as unit basis functions (B_{nLoop} and B_{tLoop}) for the stator. Fig. 3 highlights which coil in phase A is used to compute the unit basis function for the stator and its current direction.

The first step to recreate the basis function for phase A is to phase-shift B_{nLoop} and B_{tLoop} by 10° and 20° (1 and 2 slot pitches). Superimposing these functions gives the contribution from half of the windings in phase A. The second half is obtained through phase-shifting the first half by 180° and adding it to the first half. The procedure for recreating the basis function for one phase will be different, depending on stator geometry or winding configuration. However, the principle is the same: identifying a repeatable part of the windings (preferably a coil) and recreating the stator basis function from this unit function by phase-shifting and superimposing. Alternatively, generating the stator basis functions can be done by defining all the windings [7]. Different stator geometries can be defined in the FEA, which can be used for constructing a library of stator basis functions. The remaining phases are obtained by phase-shifting the basis functions by 120° and 240°. Fig. 4 shows the final stator basis functions of the studied motor with healthy windings, which can be defined as follows.

$$\begin{aligned} B_{nS}(\theta, I(t)) &= \frac{1}{I_{ref}} \sum_{k=a,b,c} I_k(t) B_{nk}(\theta) \\ B_{tS}(\theta, I(t)) &= \frac{1}{I_{ref}} \sum_{k=a,b,c} I_k(t) B_{tk}(\theta) \end{aligned} \tag{3}$$

For a machine with an ITSC in phase A, a fault can be described with the following modification written in (4).

$$\begin{aligned} B_{nS}(\theta, I(t)) &= \frac{I_a(t)}{I_{ref}} B_{nA:SC}(\theta) + \frac{I_b(t)}{I_{ref}} B_{nB}(\theta) + \frac{I_c(t)}{I_{ref}} B_{nC}(\theta) \\ &\quad + \mu \frac{I_a(t) - I_F(t)}{I_{ref}} B_{nLoop}(\theta) \\ B_{tS}(\theta, I(t)) &= \frac{I_a(t)}{I_{ref}} B_{tA:SC}(\theta) + \frac{I_b(t)}{I_{ref}} B_{tB}(\theta) + \frac{I_c(t)}{I_{ref}} B_{tC}(\theta) \\ &\quad + \mu \frac{I_a(t) - I_F(t)}{I_{ref}} B_{tLoop}(\theta) \end{aligned} \tag{4}$$

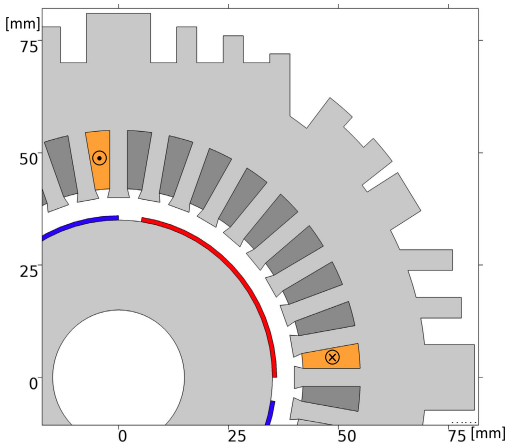

FIGURE 3. Highlighting the used coil in generating stator basis function.

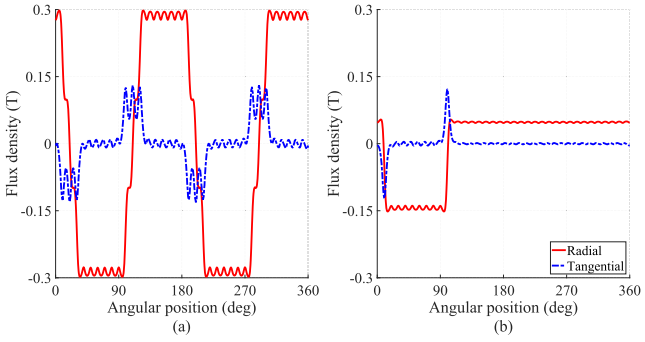

FIGURE 4. Stator basis function for (a) the recreated function for phase A and (b) one 80-turn coil.

where μ is the ratio of shorted turns in one coil and the total number of turn in that coil (i.e. 80 turns in the studied motor). It is noted that the ITSC is a local phenomenon. The block diagram in Fig. 1 illustrates how the ITSC is implemented in phase A. The location of the ITSC faults can be re-positioned by phase-shifting B_{nLoop} and B_{tLoop}. The right side of Fig. 1 illustrates how the basis function is modified in the suggested block diagram. The shorted windings are excited by the current $I_a - I_F$. An ITSC fault can be introduced to any phase, but the basis function for the fault windings needs to be phase-shifted to a valid location. The shorted windings for one phase need to be located where that phase is defined. It is not physically reasonable for an ITSC to occur in phase B if the shorted windings are located in phase C.

C. TORQUE COMPUTATION

The torque is computed by Maxwell's stress tensor (MST).

$$\tau = \frac{LR^2}{\mu_0}\int_0^{2\pi} B_T(\theta+\theta_m, I)B_N(\theta+\theta_m, I)d\theta, \tag{5}$$

where L is the length of the rotor, μ_0 is the permeability in free space, and R is the distance from the center of the motor to middle of the air-gap, where the magnetic flux density is extracted. Keeping it constant for all angular positions θ allows for a simpler expression. The torque in the developed FEA was computed with Arkkio's method.

D. FLUX LINKAGE AND ELECTROMOTIVE FORCE

It is assumed that the radial component of the magnetic flux density in the airgap goes through the stator teeth and contributes to the flux linkage.

$$\phi_i = L\int_{\frac{2\pi}{N_s}(i-1)-\frac{\pi}{N_s}}^{\frac{2\pi}{N_s}(i)-\frac{\pi}{N_s}} B_N(\theta+\theta_m, I)d\theta, \tag{6}$$

where N_s is the number of stator teeth. The following summation results in the magnetic flux linkage for each phase,

$$\lambda_n = \sum_{k=1}^{3}\sum_{i=1}^{9}\left(\phi_{i+k+3(n-1)} + \phi_{i+k+18+3(n-1)}\right) \tag{7}$$

The flux linkages for phases A, B and C are obtained by replacing n with 1, 2 or 3, respectively. Note that (7) is specific for the geometry and winding distribution of the motor model analysed in this paper. A different geometry will have a different equation, but the principle is the same, summing the magnetic flux contribution within the cross-section of the coil. The induced voltage is then computed by:

$$e_n = -C_M\frac{d\,(\lambda_n)}{dt} \tag{8}$$

The constant C_M is the geometric factor depending on the number of turns, winding distribution, motor geometry and flux leakage. In this paper, C_M was set to 3. A simple way to obtain C_M is to perform a time-step simulation at a constant speed (i.e. 1000 rpm) at no load in both FEA and FRM. The geometric factor C_M is adjusted for matching the amplitude of the excitation voltage.

E. ELECTRICAL MODEL

The electric circuit model in the abc-reference frame is used in this study [12]. This circuit allows the FRM to use a voltage input instead of a current input. In this work, the SPMSM operates in motor mode, thus the electric circuit model is shown as (9).

$$\begin{bmatrix} v_a \\ v_b \\ v_c \\ 0 \end{bmatrix} = \mathbf{R}\begin{bmatrix} i_a \\ i_b \\ i_c \\ i_F \end{bmatrix} + \mathbf{L}\frac{d}{dt}\begin{bmatrix} i_a \\ i_b \\ i_c \\ i_F \end{bmatrix} + \begin{bmatrix} e_a \\ e_b \\ e_c \\ -e_F \end{bmatrix} \tag{9}$$

where R and L are the resistance and inductance matrices given as:

$$\mathbf{R} = \begin{bmatrix} R_S & 0 & 0 & -\mu R_S \\ 0 & R_S & 0 & 0 \\ 0 & 0 & R_S & 0 \\ -\mu R_S & 0 & 0 & R_F + \mu R_S \end{bmatrix} \tag{10}$$

and

$$\mathbf{L} = \begin{bmatrix} L_S & M_S & M_S & -\mu(1-\mu)L_S \\ M_S & L_S & M_S & -\mu M_S \\ M_S & M_S & L_S & -\mu M_S \\ -\mu L_S & -\mu M_S & -\mu M_s & \mu^2 L_S \end{bmatrix} \tag{11}$$

The mutual inductance between the phase windings is neglected, but the mutual inductance between the healthy and

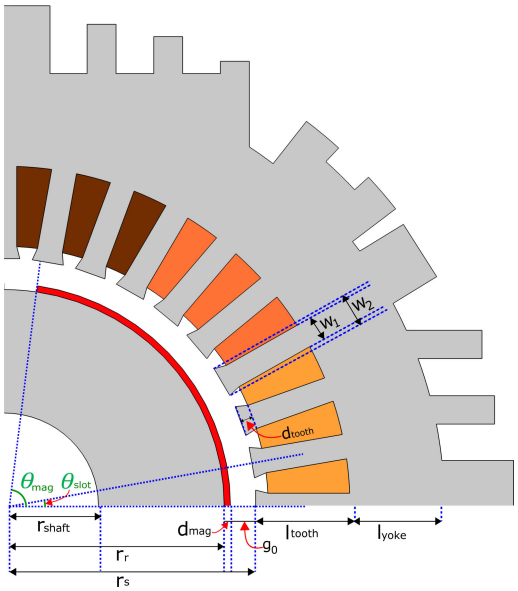

FIGURE 5. Geometry of a quarter of the studied SPMSM.

faulty windings in phase A is considered as in [13], [14]. Some entries in the matrices are divided by 6 because the ITSC is applied to only one sixth of the windings. All the excitation voltages are computed with (8), but the flux linkage for e_F is only for faulty turns. Normally, e_F can be defined to be proportional to the phase excitation voltages, depending on which phase the fault was located [13]. However, the FRM allows for computing the flux linkage in the faulty turns, being used to compute the e_F. It is also possible to estimate the back EMF constant for the motor and assume that the electromotive force is sinusoidal like in [13], but this will dismiss details in the model and reduce the model accuracy.

$$e_f = -\mu C_M \frac{d}{dt}\left(\sum_{i=2}^{10} \phi_i\right) \tag{12}$$

III. DEVELOPED FINITE ELEMENT MODEL

The motor studied in this paper is a SPMSM with concentrated windings. The motor was disassembled for measuring key geometric parameters. They are listed in Table 1 with other key parameters needed in the simulation. Only a quarter of the model is shown in Fig. 5, but the geometry of the whole motor was simulated, due to asymmetries caused by faults. The different colours (yellow, orange and brown) indicate the different phase windings (phase A, B and C) in the stator. The electromagnetic model in the FEA is defined by Maxwell's equations.

The motor is controlled by PI-controllers with an inner current loop, which controls the d- and q-components separately. The speed controller defines the reference value for the I_q, while the reference value for I_d is set as 0 A. No voltage modulation like space-vector modulation of hysteresis is included in the model. The main focus of this paper is compare the FRM with FEA when modelling faulty motors.

Fig. 6 illustrates the block diagram of the FEA model used as benchmark for the FRM. The dynamics of the mechanical parts in the model is described by a simple cylinder with applied torques and viscous friction.

$$\dot{\omega}_m = \frac{\tau - \tau_{load} - \mathrm{B}\omega_m}{J_{\mathrm{rotor}}} \tag{13}$$

The inertia of the rotor J_{rotor} and the viscose friction B are set at 0.05 $\mathrm{kg \cdot m^2}$ and 0.01 $\frac{\mathrm{N \cdot m \cdot s}}{\mathrm{rad}}$, respectively. No load torque (τ_{Load}) was required in this static FEA as mentioned earlier.

TABLE 1. Geometric dimensions and parameters of the in-house motor.

Symbol	Quantity	Parameter description
p	2	Number of pole pairs
N_s	36	Number of stator slots
N	80	Number of turns per stator slot
L_{rotor}	100 mm	Length of rotor
R	38 mm	Radius used to compute torque by MST
r_{shaft}	15 mm	Rotor inner radius
r_r	35 mm	Rotor outer radius
r_s	40 mm	Stator inner radius
d_{mag}	1 mm	Magnet thickness
g_0	4.0 mm	Average air-gap distance
L_{tooth}	14.5 mm	Length of stator tooth
d_{tooth}	2 mm	Thickness of stator tooth top
w_1	4 mm	Width of stator tooth 1
w_2	5 mm	Width of stator tooth 2
L_{yoke}	9.1 mm	Thickness of stator yoke
θ_{slot}	10°	Stator slot pitch
θ_{mag}	80.8°	Magnet pitch
n_{rated}	3000 rpm	Rated speed
k_{BEMF}	90 $\frac{\mathrm{mV}}{\mathrm{rpm}}$	Back EMF constant
R_s	2.1 Ω	Per phase resistance
L_s	36 mH	Self inductance
M_s	18 mH	Mutual inductance

The self-inductance on the real motor is 6 mH. The inductances computed in FEA is used in FRM for the best comparison between the two simulation methods.

IV. RESULTS AND DISCUSSIONS

A. COMPARISON BETWEEN FEA AND FRM

The primary purpose of this paper is to investigate the performance of the suggested FRM on modelling a faulty SPMSM with the minimum requirement for the basis functions. First, a static analysis was conducted for a comparison between FRM and FEA. The induced torque was computed in the interval 0° and 360° with 1° increments and the current excitation $I_a = 10$ A, $I_b = 0$ A, and $I_c = 0$ A. The computed torques by FEA and the proposed FRM are plotted in Fig. 7, showing an almost perfect agreement between the two methods. The faulty case is the case of a missing piece on one magnet. This verifies the validity of superimposing contributions from the rotor and stator to the magnetic field. The FEA takes 12 min 25 s to complete a simulation while the suggested FRM takes 0.103 s to compute or 7233 times faster than FEA under the same simulation requirement. This in turn is one order of magnitude larger than the existing FRM in [15]. However, the computational burden of the suggested FRM significantly increases when including the calculation of flux linkages and back EMF. This issue will be discussed

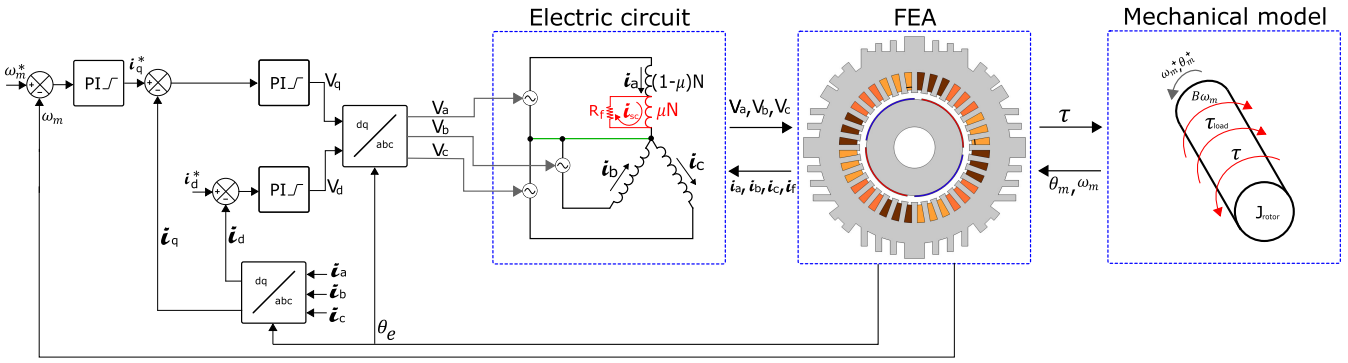

FIGURE 6. Block diagram of FE model.

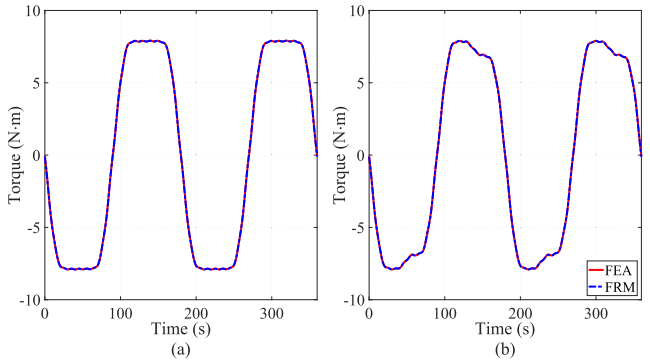

FIGURE 7. Induced torque at any rotor positions with the current excitation $I_a = 10$ A, $I_b = 0$ A and $I_c = 0$ A in (a) healthy case and (b) missing magnet piece.

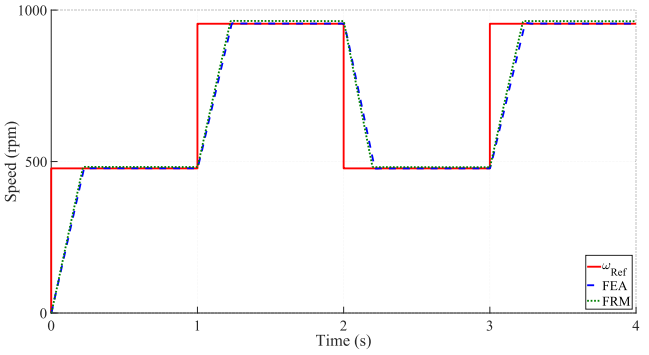

FIGURE 8. Variable speed profile of SPMSM computed by FEA and FRM in healthy case.

TABLE 2. Computation time comparison between FEA and FRM.

Fault condition	FEA	FRM	Ratio
Healthy	50906 s	49.9 s	1020
Missing magnet piece	54924 s	52.2 s	1052
ITSC (8 turns)	54877 s	49.3 s	1096
ITSC (72 turns)	55692 s	50.8 s	1080
Missing magnet piece and ITSC (8 turns)	64165 s	48.9 s	1312
Missing magnet piece and ITSC (72 turns)	64995 s	49.0 s	1326

further in detail when presenting the results of time-stepping simulations.

The second analysis is implemented with time-stepping simulations in variable speeds. The reference speed jumps between 50 rad/s and 100 rad/s as shown in Fig. 8, where only the speed prediction from the FEA and FRM in the healthy case is plotted. The speed responses from the faulty condition are close to identical. The following faults were investigated in time-stepping simulations:

- Magnet defect: A piece of a one of the north pole is removed in the middle og the magnet.
- An ITSC is applied to one of the unit coils in phase A with severity 1.7 % and 15 %. This is 1.6 % and 5.6 % of the total number of turns in phase A, respectively.
- Combination between the magnet defect and ITSC fault as previously listed.

The time-consuming computation of the FEA model with the PI-controllers is carried out for a comparative study in this paper, being listed in Table 2. The time-stepping FEA computed in 14 to 15 hours with a office laptop. Implementation of the faults in the FEA increase the computation time, due to slight changes the geometry and increased number of element in the mesh. The proposed FRM completes the time-stepping simulation in about 50 s, with the same simulation requirements like FEA. The applied fault has a little effect on the FRM computation. The ratio of computing time between FEA and the proposed FRM is also given in Table 2, indicating the difference in the computational burden. All the simulation cases studied in this paper prove that the proposed FRM is three orders of magnitude faster than FEA, verifying statements from previous published papers on FRM [15]. Furthermore, the developed FRM allows for fast extracting results of parameters, terminal voltage, armature current, torque, flux linkage, back EMF and induced search coil voltage wound around a stator tooth, and flux density from any point in the airgap. The FRM model does also have the potential to reproduce the signal of the stray flux, but it is necessary to export results from outside of the SPMSM, and not just from the airgap.

The torque is computed with different fault scenarios and plotted in Fig. 9. The suggested FRM is able to compute a similar electromagnetic torque like FEA with similar average value and level of torque ripples with the reference magnet. The reference magnet is described with a remnant magnetic flux density of 1.08 T. The missing magnet piece gives a slight decrease of torque, but the overall torque ripples are the same

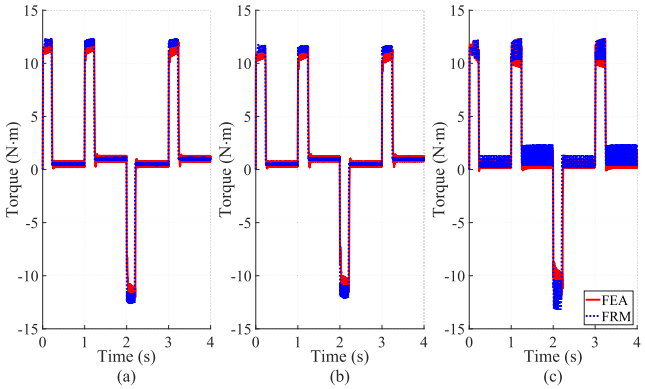

FIGURE 9. Comparison of torque estimation by FEA and FRM in case of (a) healthy motor, (b) missing magnet piece, and (c) ITSC in one coil with severity 15 %.

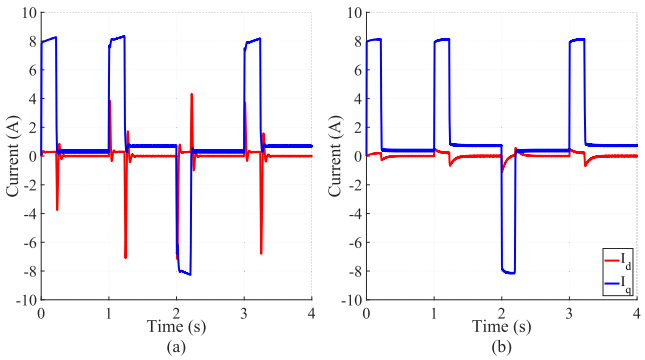

FIGURE 10. The d- and q-component of the armature current in healthy case computed by (a) FEA and (b) FRM.

in the healthy case as observed in Fig. 9a and Fig. 9b. The induced torque estimated by the FRM is close to that of FEA with an error of less than 3 %. The ITSC fault results in an increase of the torque ripples estimated by FEA and FRM, as shown in Fig. 9c. Fig. 10 shows the corresponding d- and q-components when the SPMSM is operating under healthy conditions. Both the components in FEA and FRM have a close agreement, but some spikes and dynamic responses in the FEA results were not captured by the FRM. However, SPMSMs are usually fed by a well-controlled converter, allowing for limiting such spikes in a current regulator.

An ITSC was applied to one coil in phase A with the severity levels of 1.7 % (8 turns) and 15 % (72 turns). The short circuit current I_{sc}, which is equal to the difference between I_a and I_F, flowing through the fault resistor R_F is plotted in Fig. 11. The predicted I_{sc} by FRM is close to that of FEA in the severe case, but less agreed in the lower severity. Results from the FRM are time-shifted slightly for better highlighting the similarity between the current waveforms. Minor differences in the induced torque cause the peaks imperfectly in phase. The simplified electrical model probably is the main reason behind the deviation from FEA in less severe ITSC faults. RMS of I_{sc} is not deviated significantly between the two models. However, I_{sc} is not a suitable fault indicator in fault diagnosis, because typically only in-house tests or numerical simulations have the possibility of estimating this

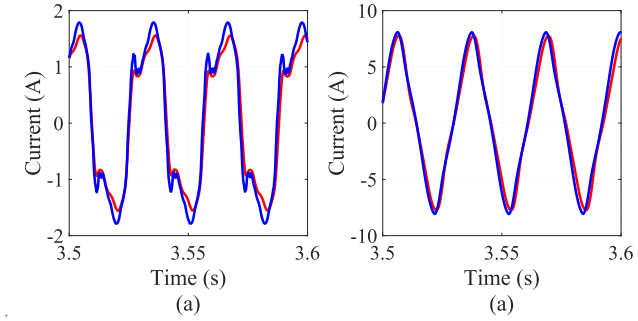

FIGURE 11. Short circuit current I_{sc} in case of ITSC in one coil with severity (a) 1.7 % and (b) 15 %.

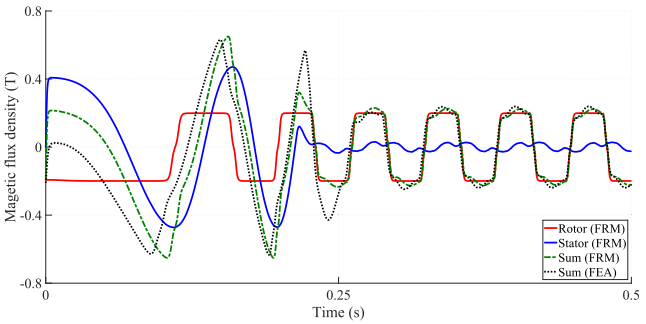

FIGURE 12. Decoupling the contribution to the radial component of the air-gap magnetic flux density from the rotor and stator in case of no fault and comparison between FRM and FEA.

quantity [14], [16]. Conventionally, SPMSM drives cannot measure I_{sc}, but the presented result aims at confirming of the FRM's capabilities of reproducing the results from FEA.

B. FAULT INDICATORS IDENTIFIED BY FRM

The radial and tangential components of the magnetic flux density in the air-gap in the healthy case are plotted in Fig. 12 for the first half second of the time-stepping simulations, proving that the FRM can easily decouple the contribution to air-gap flux given by rotor and stator. During the acceleration within the first 0.25 s, the contribution from the stator field is more dominating than that from the rotor. However, the magnitude decreases when the motor reaches a constant speed of 478 rpm (50 rad/s), but would increase again if the motor needs to change speed or if load is applied to the rotor. The sum of the field contributions shows a close agreement with the result from FEA, both in magnitude and shape of the waveform.

The magnets of the SPMSM are defined with a constant remnant magnetic flux, resulting in the radial component of the magnetic flux density contributed by the rotor as a trapezoidal shape or red curve in Fig. 12a. Therefore, a flux sensor located in air-gap can track the shape of the magnetic flux density at no load conditions, and compare the shape in later operations. If the shape begins to deviate over time, a magnet defect can be detected. In case of magnet defects like missing magnet piece or partial demagnetisation, this may appears as a period dip in the trapezoidal waveform as shown in Fig. 13. This is the same principle as using search

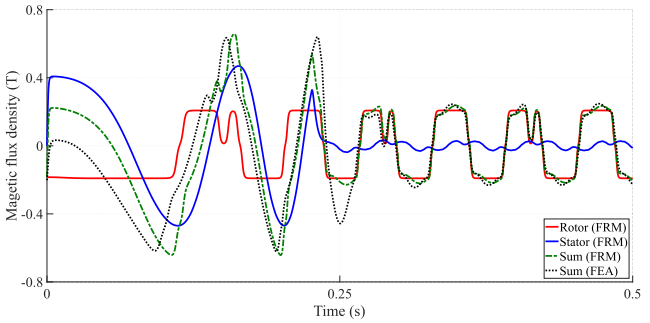

FIGURE 13. Decoupling the contribution to the normal component of the air-gap magnetic flux density from the rotor and stator in the case of missing magnet piece and comparison between FRM and FEA.

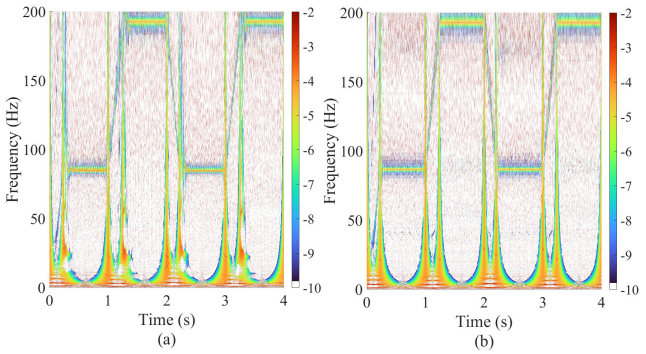

FIGURE 14. Spectrogram of I_P in log scale with missing magnet piece computed in (a) FEA and (b) FRM.

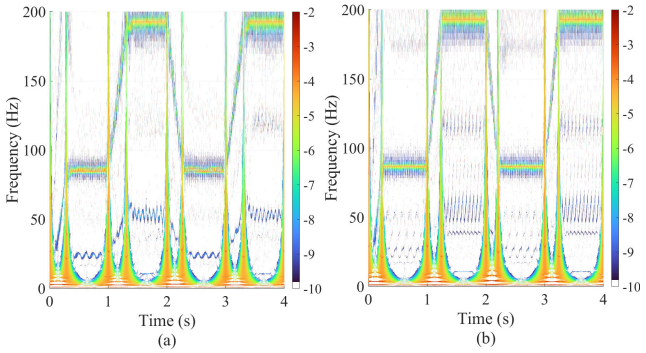

FIGURE 15. WSST of amplitude of state space vector I_S in log scale with both 8 shorted turns and missing magnet piece. Computed in (a) FEA and (b) FRM.

coil for detecting magnet faults as described in [17]. A magnet defect like partial demagnetisation can be decoded with only one sensor. Other asymmetries in the magnetic circuit like eccentricity would need at least a minimum two sensors.

Stator short-circuit faults in electrical machines are often detected by an increase of the third harmonic of the armature current. Within this work, the extended Park's vector approach (EPVA) [18] is chosen. Stator currents are extracted from the proposed FRM and used to compute the Park's vector. The magnitude of the Park's vector, $|I_P|$, is used in a time-frequency analysis and is defined as

$$|I_P| = \sqrt{I_\alpha^2 + I_\beta^2} \tag{14}$$

where I_α and I_β are the components of the stator current vector in the stationary reference frame (α, β). Under an ITSC, the second harmonic of the current space vector increases in the spectrogram obtained by the wavelet synchronised transformation (WSST) [18]. In case of missing magnetic, no second harmonic is visible in the Fig. 14.

Fig. 15 shows the results from the simulation where the SPMSM has 8 shorted turns and missing magnet piece. The second harmonic is present at the frequencies 32 Hz and 64 Hz, depending on the motor speed profile in Fig. 8. This highlights the $2 \cdot f_s$ peak in Fig. 15, which is not present in either of the subfigures in Fig. 14. Missing magnet piece does not generate thus second harmonic, thus it is caused by the ITSC fault. The amplitude of the second harmonic becomes more viable when the severity of ITSC fault increases. The result in Fig. 15 confirms the efficacy of the EPVA and shows that magnet defects has little effect on the second harmonic.

The developed FRM in this work focuses on 2 electrical faults in PMSMs, namely demagnetisation and ITSC, which were not addressed in literature. FRMs can also be modified for other fault types like high resistance connection, line-to-line short circuit, phase-to-ground short circuit and eccentricities faults as discussed in [8].

C. EXPERIMENTAL VALIDATION

Experimental validations were conducted on a 4-pole 2.2 kW SPMSM of an in-house test setup. The motor is coupled to a generator (3 kW 4-pole SPMSM) with a torque sensor in between. The generator is wye-connected to a three-phase restive load. Fig. 16 shows an overview of the in-house test bench. The whole setup was controlled via a Dspace controller installed on office laptop. The Microlabbox sent out the control signal to the ABB commercial drive and record signals of torque, current, and position. The sensors were powered by the 24 V DC-power supply. The test motor got multiple taps that can be used for ITSC. The available severity are 2 %, 5 % and 6 %. The taps related for each specific fault severities were connected to an external fault resistor (1 Ω). It makes the artificial ITSC more realistic, since it represents the degeneration of the insulation and limits the fault current. The current through the fault resistor reached 6.4 A at nominal speed in no-load condition.

The motor was run at 1500 rpm and 3000 rpm (nominal speed), at 50 % of rated load. The load was estimated by the ABB-drive. The loading condition was increased by decreasing the resistance in the resistor bank. First, no ITSC was implemented on the motor. Measurements were recorded for 120 s at a sampling frequency of 10 kHz. The motor was stopped for safe rewiring and implementation the ITSC. The resistance of the resistor bank was also increased to the maximum when increasing the steady-state speed from 1500 rpm to 3000 rpm since a larger speed translates to larger output load when the resistance is kept constant. Identical scenarios were simulated in the FRM. The results of the chosen fault indicator, second harmonic of I_P is presented in Table 3, being obtained by fast Fourier transform of two

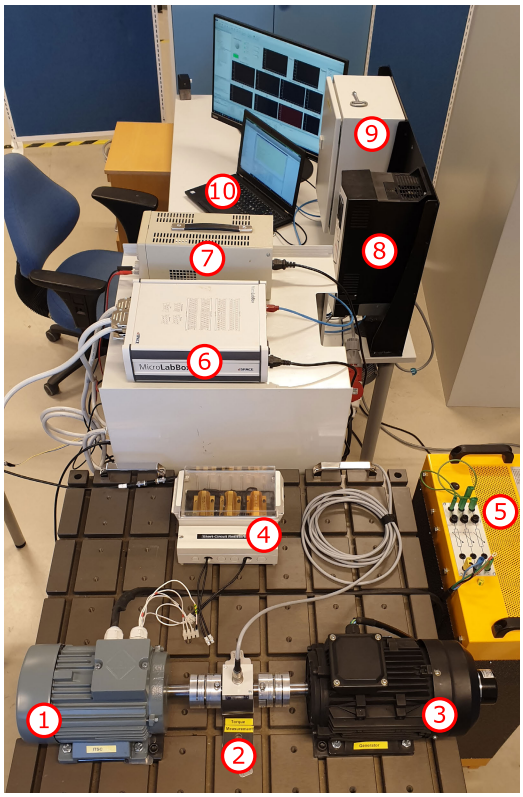

FIGURE 16. In-house test setup with (1) motor, (2) torque sensor, (3) generator, (4) fault resistor, (5) resistor bank, (6) Microlabbox, (7) low voltage DC-supply, (8) ABB motor drive, (9) cabinet containing current sensors, and (10) laptop.

TABLE 3. Amplitude of second harmonic of $|I_P|$ at different short circuit serveries.

ITSC	1500 rpm	3000 rpm
0 %	-48.7 dB	-47.8 dB
2 %	-46.0 dB	-46.7 dB
5 %	-46.1 dB	-45.5 dB
6 %	-46.3 dB	-44.6 dB

minutes long measurements, which were normalised by their respected DC-component of I_P. The general trend is that the second harmonic is increasing with increasing severity of ITSC, but the trend has a greater slope at higher speed.

The spectrograms of the I_P in cases of 0 % and 6 % at nominal speed are presented in spectrograms of Fig. 17. The simulation shows that the second harmonic of I_P will increase by 4.4 dB when a short circuit is implemented. This is also shown in the experimental measurement where the second harmonic increased by 3.2 dB. It is noted that the obtained result by FRM has a lower noise level than the experimental data, but does show the general trend of the chosen fault indicator [18].

V. CONCLUSION

This paper develops a field reconstruction model to model faults in SPMSM. The key features of the new model includes a developed magnet library and the implementation of ITSC in FRM. The developed model can simulate magnet defects, ITSC and has the potential to easy implement both faults in

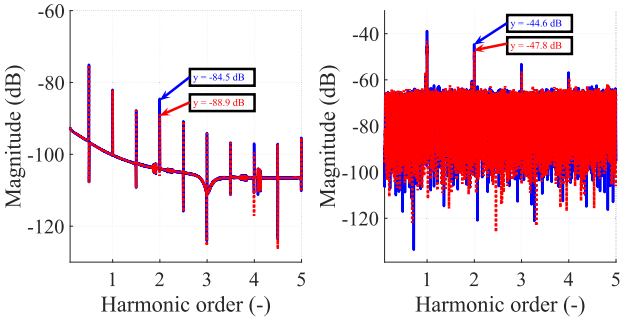

FIGURE 17. Comparison between spectrogram of I_P obtained from (a) FRM or (b) experiment.

the same simulation. Further, the model can present detailed results of current, terminal voltage, EMF, torque, flux linkage, stator tooth flux density and induced search coil voltage.

The model presented in this paper performed over 1000 times faster than the compared commercial FEA and was able to reproduce signals that can be analysed with fault indicator for magnet defects and ITSC. If the model did not include the computation of flux linkages and EMF, it is over 7000 times faster. Therefore, the integration of the flux linkage increases computational burden significantly. This faster computing FRM (without computation of flux linkage and EMF) may have potential for developing condition monitoring of torque or magnetic flux density.

REFERENCES

[1] J. Luznar, J. Slavič, and M. Boltežar, "Structure-borne noise at PWM excitation using an extended field reconstruction method and modal decomposition," *Strojniski Vestnik J. Mech. Eng.*, vol. 65, no. 9, pp. 471–481, Sep. 2019.

[2] M. Kiani, D. Torregrossa, B. Fahimi, F. Peyraut, and A. Miraoui, "Detection of faults in PMSM using field reconstruction method and mechanical impulse response," in *Proc. 26th Annu. IEEE Appl. Power Electron. Conf. Expo. (APEC)*, Fort Worth, TX, USA, Mar. 2011, pp. 1896–1901. [Online]. Available: http://ieeexplore.ieee.org/document/5744854/

[3] B. Fahimi and A. Khoobroo, "Method and apparatuses for fault management in permanent magnet synchronous machines using the field reconstruction method," U.S. Patent 8 314 576 B2, Nov. 20, 2012. [Online]. Available: https://patents.google.com/patent/US8314576B2/en

[4] A. Khoobroo and B. Fahimi, "Magnetic flux estimation in a permanent magnet synchronous machine using field reconstruction method," *IEEE Trans. Energy Convers.*, vol. 26, no. 3, pp. 757–765, Sep. 2011. [Online]. Available: https://ieeexplore.ieee.org/document/5776667

[5] B. J. Deken and S. D. Pekarek, "Enhanced field reconstruction method for the efficient analysis of permanent magnet synchronous machines," *IEEE Trans. Energy Convers.*, vol. 27, no. 3, pp. 661–669, Sep. 2012. [Online]. Available: https://ieeexplore.ieee.org/document/6236115

[6] L. Gu, S. Wang, D. Patil, B. Fahimi, and M. Moallem, "An improved conformal mapping aided field reconstruction method for modeling of interior permanent magnet synchronous machines," in *Proc. IEEE Energy Convers. Congr. Expo. (ECCE)*, Milwaukee, WI, USA, Sep. 2012, pp. 1–7. [Online]. Available: https://ieeexplore.ieee.org/document/7854845

[7] P. Chen, T. Chen, J. Liang, B. Fahimi, and M. Moallem, "Torque ripple mitigation via optimized current profiling in interior permanent magnet synchronous motors," in *Proc. IEEE Int. Electr. Mach. Drives Conf. (IEMDC)*, San Diego, CA, USA, May 2019, pp. 240–247. [Online]. Available: https://ieeexplore.ieee.org/document/8785352

[8] D. Torregrossa, A. Khoobroo, and B. Fahimi, "Prediction of acoustic noise and torque pulsation in PM synchronous machines with static eccentricity and partial demagnetization using field reconstruction method," *IEEE Trans. Ind. Electron.*, vol. 59, no. 2, pp. 934–944, Feb. 2012. [Online]. Available: https://ieeexplore.ieee.org/document/5764527

[9] A. Khoobroo and B. Fahimi, "A new method of fault detection and treatment in five phase permanent magnet synchronous machine using field reconstruction method," in *Proc. IEEE Int. Electr. Mach. Drives Conf. (IEMDC)*, Miami, FL, USA, May 2009, pp. 682–688. [Online]. Available: https://ieeexplore.ieee.org/document/5075279
[10] W. Zhu, B. Fahimi, and S. Pekarek, "A field reconstruction method for optimal excitation of permanent magnet synchronous machines," *IEEE Trans. Energy Convers.*, vol. 21, no. 2, pp. 305–313, Jun. 2006. [Online]. Available: https://ieeexplore.ieee.org/document/1634576
[11] Y. Park, D. Fernandez, S. B. Lee, D. Hyun, M. Jeong, S. K. Kommuri, C. Cho, D. D. Reigosa, and F. Briz, "Online detection of rotor eccentricity and demagnetization faults in PMSMs based on Hall-effect field sensor measurements," *IEEE Trans. Ind. Appl.*, vol. 55, no. 3, pp. 2499–2509, May 2019.
[12] B. Vaseghi, B. Nahid-Mobarakeh, N. Takorabet, and F. Meibody-Tabar, "Experimentally validated dynamic fault model for PMSM with stator winding inter-turn fault," in *Proc. IEEE Ind. Appl. Soc. Annu. Meeting*, Edmonton, AB, Canada, Oct. 2008, pp. 1–5. [Online]. Available: https://ieeexplore.ieee.org/document/4658812?section=abstract
[13] Y. Qi, E. Bostanci, V. Gurusamy, and B. Akin, "A comprehensive analysis of short-circuit current behavior in PMSM interturn short-circuit faults," *IEEE Trans. Power Electron.*, vol. 33, no. 12, pp. 10784–10793, Dec. 2018. [Online]. Available: https://ieeexplore.ieee.org/document/8302979
[14] Y. Qi, E. Bostanci, M. Zafarani, and B. Akin, "Severity estimation of interturn short circuit fault for PMSM," *IEEE Trans. Ind. Electron.*, vol. 66, no. 9, pp. 7260–7269, Sep. 2019.
[15] D. Torregrossa, B. Fahimi, F. Peyraut, and A. Miraoui, "Fast computation of electromagnetic vibrations in electrical machines via field reconstruction method and knowledge of mechanical impulse response," *IEEE Trans. Ind. Electron.*, vol. 59, no. 2, pp. 839–847, Feb. 2012. [Online]. Available: https://ieeexplore.ieee.org/document/5754577
[16] J. C. Urresty, J. R. Riba, and L. Romeral, "Diagnosis of interturn faults in PMSMs operating under nonstationary conditions by applying order tracking filtering," *IEEE Trans. Power Electron.*, vol. 28, no. 1, pp. 507–515, Jan. 2013. [Online]. Available: https://ieeexplore.ieee.org/document/6198360
[17] Z. Ullah and J. Hur, "A comprehensive review of winding short circuit fault and irreversible demagnetization fault detection in PM type machines," *Energies*, vol. 11, no. 12, p. 3309, Nov. 2018. [Online]. Available: https://www.mdpi.com/1996-1073/11/12/3309
[18] P. Pietrzak and M. Wolkiewicz, "Comparison of selected methods for the stator winding condition monitoring of a PMSM using the stator phase currents," *Energies*, vol. 14, no. 6, p. 1630, 2021. [Online]. Available: https://www.mdpi.com/1996-1073/14/6/1630

SVEINUNG ATTESTOG received the B.Sc. and M.Sc. degrees in renewable energy from the University of Agder, Grimstad, Norway, in 2016 and 2018, respectively. He is currently working as a Ph.D. Research Fellow in mechatronics. His main research interests include applied signal processing and fault detection of PMSM in transient operating conditions.

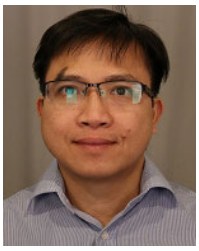

HUYNH VAN KHANG received the B.Sc. degree in electrical engineering from Ho Chi Minh City University of Technology, Ho Chi Minh City, Vietnam, in 2002, the M.Sc. degree in electrical engineering from Pusan National University, Busan, South Korea, in 2008, and the D.Sc. (Tech.) degree in electrical engineering from Aalto University, Espoo, Finland, in 2012. From 2013 to 2019, he was an Associate Professor of electrical power engineering with the University of Agder, Grimstad, Norway, where he is currently a Professor with the Department of Engineering Sciences. His research interests include electrical machines, condition-based maintenance, and applied power electronics.

KJELL G. ROBBERSMYR (Senior Member, IEEE) received the M.Sc. and Ph.D. degrees in mechanical engineering from the Norwegian University of Science and Technology, Trondheim, Norway, in 1985 and 1992, respectively. He was the Head of the Dynamics Research Group. He is currently the Director of the Mechatronics Research Centre, University of Agder, Grimstad, Norway. He is a Professor of machine design. His main research interests include machine design, rotating machines, condition monitoring, and vehicle crash simulations.